Numerical Study on the Effect of Pressure on Biodiesel/N-Pentanol Blended Droplet Homogeneous Micro-Explosion

Kai Han [1,a] and Minghou Liu [1,*]

[1]Department of Thermal Science and Energy Engineering, University of Science and Technology of China, Hefei 230026, China

Abstract. A three-dimensional droplet evaporation model using VOF is developed to study the influence of pressure on biodiesel/n-pentanol blended droplet homogeneous nucleation and evaporation characteristics. Numnerical results reveal that the homogeneous nucleation ratereduces while the homogeneous superheating limit temperature increases with increase of the pressure and the critical n-pentanol mole fraction. The minimum n-pentanol mole fraction of 0.65 is required for homogeneous nucleation when the ambient pressure is 12 atm. Higher pressure also weakens surface evaporation of droplets, which reduces the increase rate of vapor concentration around droplets, and increases the peak vapor value. The homogeneous micro-explosion can only occur when the ambient pressure is greater than 3 atm. As pressure increases, the temperature and temperature rise rate of droplets increases, and the homogeneous micro-explosion delay reduces.

1 Introduction

The evaporation characteristics of liquid droplets have always been a hot research topic. Law [1] proposed an evaporation model based on the Infinite Conduct Model (ICM), in which temperature changes with time but does not be influenced by the internal position of the droplet. Later, the Finite Conduct Model (FCM) was developed to consider the variation of internal temperature of droplets with position [2]. Abramzon [3] considered the effect of internal circulation on the droplet evaporation and introduced the Effective Eonductivity Model (ECM) using a corrected thermal conductivity. However, the above models are limited to single component droplets.

Bhattacharya et al. [4] conducted theoretical research on binary droplets composed of n-hexane and n-hexadecane. Their research includes the effects of limited diffusion and rapid mixing on droplet evaporation. Sezen [5] derived an analytical expression for a single multi-component droplet based on the Infinite Conduction Model (ICM). Zeng et al. [6] used a third-order polynomial to model the temperature and concentration distributions of multi-component fuel film vaporization. Nadykto et al. [7] derived mass flux expressions for the multi-component droplet evaporation and condensation under non-isothermal conditions. Sazhin's team has reported numerous studies on the multi-component droplet evaporation [8, 9]. In the above studies, however, the influence of droplet deformation was not considered.

Banerjee used VOF numerical study to investigate the evaporation characteristics of binary blended droplets composed of ethanol and iso-octane [10], taking into account the deformation of droplets. However, the change of physical properties with temperature is not consdiered. Strotos et al. [11] conducted a detailed study on the temperature and concentration field changes during the evaporation process of n-heptane and n-decane blended droplets, and used grid adaptive technology and VOF to consider the deformation of droplets, including the influence of temperature on physical properties. However, a two-dimensional model was used, and the actual three-dimensional droplet evaporation needs to be studied.

To sum up, the shortcomings of current research on droplet evaporation are: First, the mechanism by which ambient pressure affects droplet evaporation is not clear. Second, the mechanism is not clear whether droplets can form homogeneous micro-explosions during the evaporation process and the conditions for forming homogeneous micro-explosions. Therefore, this paper uses a three-dimensional VOF model to study droplet evaporation, analyzes in detail the influence of ambient pressure on droplets evaporation, and explores the conditions for homogeneous micro-explosions to occur. Considering the strong renewability, biodiesel [12-23] and n-pentanol [14, 24-27] blended droplets are selected in this study.

* Corresponding author: mhliu@ustc.edu.cn
[a] xhk@mail.ustc.edu.cn

2 Simulation model

2.1 Governing equation

Volume of fluid (VOF) is used to study the evaporation characteristics of biodiesel and n-pentanol droplets at different ambient pressures. The governing equations are as follows:

2.1.1 Continuity equation

$$\frac{\partial}{\partial t}\left(\alpha_q \rho_q\right)+\nabla\cdot\left(\alpha_q \rho_q \vec{v}_q\right)=S_{\alpha_q} \tag{1}$$

In the formula, q is the q phase, ρ represents the density, $\vec{v}_q$ represents the velocity, $S_{\alpha q}$ represents the source term and is determined by the evaporation rate of the liquid. α is the volume fraction, which satisfies the following relationship:

$$\sum_{q=1}^{n}\alpha_q=1 \tag{2}$$

Where n represents the number of phases in multiphase flow. In this study, n=2, and the fluid in the computational domain is composed of two phases: liquid droplets and gas. The second phase is solved using Equation (1), while the volume fraction of the main phase is solved using Equation (2). If α_q=0, the cells are filled with liquid; if α_q=1, the cells are filled with gas; if 0<α_q <1, the grid cells belong to the phase interface. Specifically, this study defines the cells with α_q=0.5 as the droplet surface.

2.1.2 Momentum equation

$$\frac{\partial}{\partial t}(\rho\vec{v})+\nabla\cdot(\rho\vec{v}\vec{v})=-\nabla p+\nabla\cdot[\mu(\nabla\vec{v}+\nabla\vec{v}^{T})]+\rho\vec{g}+\vec{F} \tag{3}$$

In the formula, $\vec{g}$ and $\vec{F}$ represent gravitational acceleration and volumetric force, μ and p represent viscosity and grid cell pressure, respectively.

In addition, the surface tension σ is expressed as a volumetric force and added to the momentum equation as a source term using the continuous surface force (CSF) model:

$$F_{vol}=\sigma_{ij}\frac{\rho\kappa_i\nabla\alpha_i}{\frac{1}{2}(\rho_i+\rho_j)} \tag{4}$$

$\nabla\alpha$ and ρ are the volume fraction gradient and density, κ is curvature.

$$\hat{n}=\hat{n}_w\cos\theta_w+\hat{t}_w\sin\theta_w \tag{5}$$

In this paper, the contact angle between the droplet and the suspension medium was 30°. As shown in Equation(5), the contact angle in the VOF model is mainly used to adjust the surface normal vector direction of cells near the wall, where $\hat{n}_w$ represents the unit vector perpendicular to the wall and $\hat{t}_w$ represents the unit vector tangent to the wall.

2.1.3 Energy equation

$$\frac{\partial}{\partial t}\left(\rho E\right)+\nabla\cdot\left[\vec{v}\left(\rho E+p\right)\right]=\nabla\cdot\left(k_{eff}\nabla T\right)+S_h \tag{6}$$

The energy in Equation (6) is defined Equation (7). In Equation (6), k_{eff} is the effective thermal conductivity. S_h is the energy source term caused by the evaporation of liquid components.

$$E=\frac{\sum_{q=1}^{n}\alpha_q\rho_q E_q}{\sum_{q=1}^{n}\alpha_q\rho_q} \tag{7}$$

The energy E_q of each phase in Equation (7) is determined by its specific heat capacity and temperature.

2.1.4 Species equation

$$\frac{\partial\left(\alpha_q\rho_q Y_q^i\right)}{\partial t}+\nabla\cdot\left[\alpha_q\rho_q\vec{v}_q Y_q^i\right]=-\nabla\cdot\left(\alpha_q\vec{J}_q^i\right)+\alpha_q S_q^i \tag{8}$$

$$\sum_{i=1}^{n}Y_q^i=1 \tag{9}$$

In the formula, $Y_q^i$is the mass fraction, $\vec{J}_q^i$ is the flow rate and S_q^i is the net generation rate of component i in q phase. The gas phase consists of n-pentanol, biodiesel and nitrogen gas. The mass fractions of n-pentanol and biodiesel vapor are solved by Equation (8), while the mass fraction of nitrogen is solved by Equation (9) based on the solution of Equation (8). The liquid phase consists of n-pentanol and biodiesel liquid. Similarly, the mass fraction of n-pentanol liquid is obtained by solving Equation (8), while the mass fraction of biodiesel liquid is obtained by solving Equation (9) after obtaining the mass fraction of n-pentanol liquid.

2.1.5 Heat conduction equation

Heat exchange occurs between the thermocouple wire and the droplet, as well as between the thermocouple wire and the gas, through conjugate heat transfer. Based on Equation (6), the temperature governing equation in the thermocouple wire is as follows:

$$\frac{\partial}{\partial t}\left(\rho E\right)=\nabla\cdot\left(k_{eff}\nabla T\right)+S_h \tag{10}$$

There is no longer any convective term affecting

energy transport in the solid region.

2.2 Physical properties

The biodiesel and n-pentanol used in this study are described in reference [28]. The changes in liquid and vapor properties of n-pentanol, methyl palmitate, methyl stearate, methyl oleate, and methyl linoleate with temperature are derived from Aspen Plus. As shown in Equation (11), the physical properties of biodiesel liquid and vapor are the mass fraction average of pure components, where ϕ_b is the physical properties of biodiesel liquid and vapor, ϕ_i and Y_i represent the physical properties and mass fraction of pure components, respectively.

$$\phi_b = \sum_i \phi_i Y_i \tag{11}$$

The physical properties of the liquid phase blends are the mass fraction average of n-pentanol and biodiesel liquid, while the physical properties of the gas phase blends are the mass fraction average of n-pentanol vapor, biodiesel vapor, and nitrogen. In Equation (12), ϕ_q represents the physical properties of q phase, $\phi_q^i$and Y_q^i represent the physical properties and mass fraction of the i component in q phase.

$$\phi_q = \sum_i \phi_q^i Y_q^i \tag{12}$$

Due to the adoption of the VOF model, the physical properties of the cells are determined by the physical properties and volume fraction of each phase in the cell, and the calculation formula is shown in Equation (13). In the equation, ϕ represents the physical properties of the cells, and α_q represents the volume fraction of q phase.

$$\phi = \sum_q \phi_q \alpha_q \tag{13}$$

2.3 Phase change model

$$m_j''' = -k\alpha_l \rho_g D_{\text{eff}}^j \nabla y^j \cdot \nabla \alpha_g \tag{14}$$

m_j''' is the amount of j component generated in the gas phase per unit time and unit volume within the surface grid cells of the droplet, which is the evaporation amount of i component in the liquid phase. $\nabla\alpha_g$ and ρ_g are the volume fraction gradient and density of the gas phase. D_{eff}^j and ∇y^j are the diffusion coefficient and mass fraction gradient of component j. As mentioned earlier, the gas-liquid interface with α_g=0.5 is taken as the droplet surface, which means that evaporation only occurs within the grid cells where the volume fraction of the liquid phase is $0<\alpha_l\leq 0.5$. Therefore, α_l is added to Equation (14) to identify the cells where evaporation occurs. Besides, k is added as an adjustment coefficient based on experimental data.

2.4 Homogeneous nucleation model

When the liquid component reaches the superheating limit temperature, homogeneous nucleation will occur. The Avedisian-Glassman model is used here, and the calculation equation for the homogeneous nucleation rate $J(T_l)$ is as follows [29-31]:

$$J(T_l) = N_0 k_f \Gamma \cdot \exp\left(-\frac{\Delta A^*}{k_B T_l}\right) \tag{15}$$

In the formula, Γ is the adjustment coefficient, which is taken as 1. k_B represents the Boltzmann constant, which is 1.38×10^{-23}. T_l is the temperature of the liquid; N_0 is the molecular number density; ΔA^* is the molecular free energy, and k_f is the molecular collision frequency. N_0, ΔA^* and k_f are calculated by Equations (16)-(17), respectively:

$$N_0 = \frac{\rho}{M} N_A \tag{16}$$

$$\Delta A^* = \frac{16\pi\sigma^3}{3(P_g - P_l)^2}. \tag{17}$$

$$k_f = \frac{8P_g\sigma^2}{\left(P_g - P_l\right)^2}\left(\frac{2\pi}{k_B T_l}\right)^{1/2} \sum_k \left(\frac{Y_{gz}}{M_z^{1/2}}\right) \tag{18}$$

N_A is the Avogadro number, which is 6.02×10^{23}; ρ is density and σ is surface tension. P_g is the saturated vapor pressure of the bubble; P_l is the pressure of the liquid; Y_{gz} is the mass fraction of the z component in the gas phase, and M_z is the mole mass of the z component. The calculation methods for density, surface tension, saturated vapor pressure, and gas mass fraction are as described earlier.

2.5 Computational domain and dynamic mesh

2.5.1 Computational domain and boundary conditions

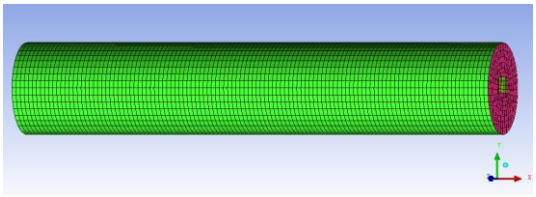

Fig. 1. Schematic diagram of computational domain.

As shown in Fig. 1, the computational domain is cylindrical with a length of 350 mm and a radius of 32 mm. The left and right faces respectively represent the Pressure-outlet conditions, where the outlet pressure is the pressure of the studied operating condition. The cylindrical side is a wall condition. The temperature distribution at the boundary and the initial temperature distribution of the computational domain vary linearly with the coordinate change in the droplet movement

direction (x-axis). In addition, in order to reduce the grid number and save computational costs, the multi-domain grid is used and the grid is refined locally.

In Fig. 2, the fluid regions Fluid3 (350 mm×11 mm ×16 mm) and Fluid4 are structured mesh with a mesh size of 3 mm, and their boundaries are connected by an interface pair. The fluid region Fluid2 (6 mm×11 mm× 16 mm) is an unstructured mesh with a maximum mesh size of 3 mm, connected to Fluid3 and Fluid4 through interface pairs. In addition, Fluid2 serves as a motion domain and transports droplets from the left low-temperature environment to the right high-temperature environment through dynamic mesh technology. Fluid3 can be understood as a channel designed for the dynamic mesh.

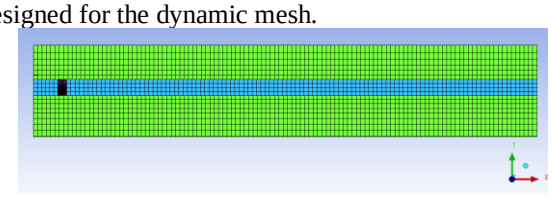

Fig. 2. Schematic diagram of local computation domain.

As shown in Fig. 3, in order to reduce post-processing costs, a fluid region Fluid1 (with a radius of 2.5 mm) is designed in the fluid region Fluid2, connected to Fluid2 through the Interior boundary, with a maximum grid size of 1 mm. The medium of the solid area (radius of 0.1 mm, length of 2 mm) is the nickel-chromium alloy, with a maximum grid size of 0.085 mm. It is connected to Fluid1 and Fluid2 through the Coupled wall to suspend droplets. The central area of Fluid1 has been refined with a radius of 1 mm to initialize the droplet. The grid independence verification will be conducted on the central refined area of Fluid1.

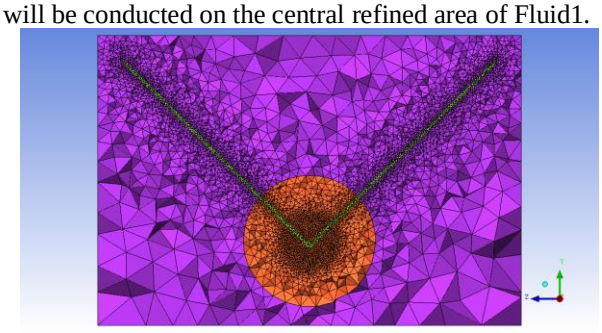

Fig. 3. Fluid2 schematic diagram.

2.5.2 Dynamic mesh technology

Layering can ensure the quality of updated grid cells with less computational complexity. Therefore, this study adopts the dynamic layering method, and the specific principle is as follows:

$$h_{min} > (1+\alpha_s)h_{ideal} \tag{19}$$

$$h_{min} < \alpha_c h_{ideal} \tag{20}$$

In the equations, α_s is the splitting factor, and α_c is the collapse factor, with values of 0.4 and 0.2 respectively. The h_{ideal} value is 3 mm. During the motion, Fluent automatically detects the height h_{min} of the grid cells connected to the motion boundary. When in the stretched state, the grid cell splits into two new grid cells if h_{min} satisfies Equation (19); when in the compressed state, the grid cells are merged into a new grid cell if h_{min} satisfies (20).

2.6 Model validation

2.6.1 Grid independence

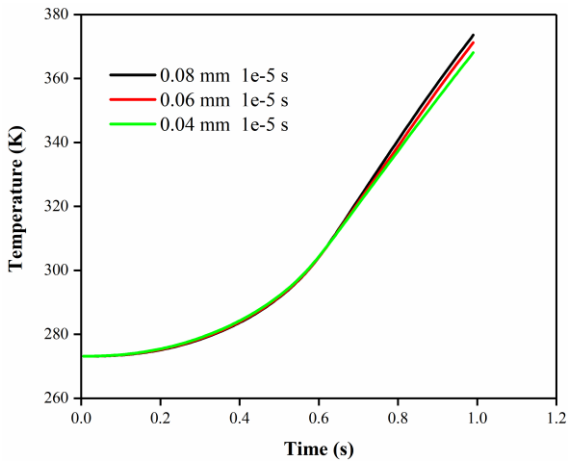

Fig. 4. Grid independence.

Fig. 4 shows the change of the droplet average temperature during the movement process with time and grid size at a time step of 1×10^{-5} s. As shown in Fig. 3, grid independence is performed on the central refined area of Fuid1. Fig. 4 shows that when the maximum grid size decreases in an arithmetic sequence of 0.08 mm, 0.06 mm, and 0.04 mm, the droplet average temperatures at the pre-set heating position are 373.61 K, 371.26 K, and 368.10 K, respectively. The relative errors of the changes are 0.63% and 0.85%, both less than 1%. The errors are within the acceptable range. Considering the computational cost, this study selects a grid with a maximum grid size of 0.06 mm.

2.6.2 Time step independence

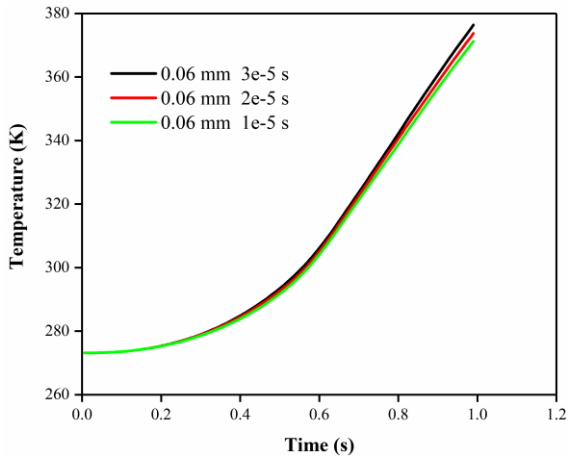

Fig. 5. Time step independence.

The change of the droplet average temperature with time and different time steps at a maximum grid size of 0.06 mm is shown in Fig. 5. When the time step decreases in an arithmetic sequence of 3×10^{-5} s, 2×10^{-5} s, and 1×10^{-5} s, the droplet average temperatures at the pre-set heating position are 376.40 K, 373.70 K, and 371.26 K, with relative errors of 0.71% and 0.65%, respectively. The relative errors caused by the change in time step are less than 1%. Considering the computational cost, the time step of this study is selected as 0.00003 s. It is emphasized here that throughout the entire calculation process, three types of time steps can all ensure that the Courant number is less than 1.

2.6.3 Data verification

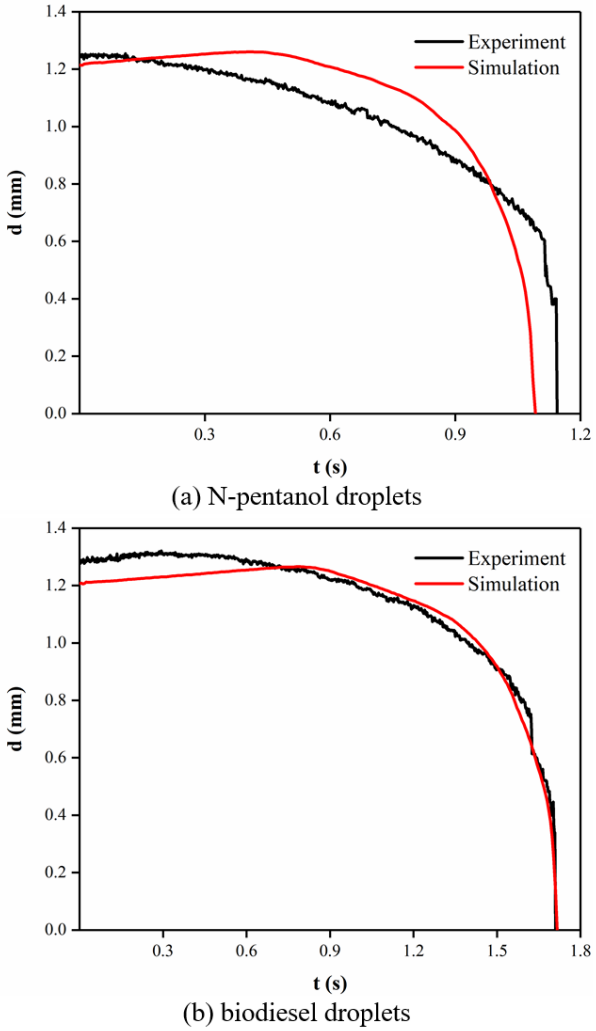

Fig. 6. data verification.

The numerical and experimental diameter of N-pentanol and biodiesel droplets with time are shown in Fig. 6. It should be noted that due to numerous uncontrollable disturbances during the droplet evaporation experiment, the simulation result curve and the experimental result curve cannot completely match. According to Fig. 6, the errors between the simulation result and the experimental result is acceptable when the evaporation coefficient k_b of biodiesel is set to 0.34, and the evaporation coefficient k_p of n-pentanol is set to 0.12.

3 Results and discussion

3.1 Homogeneous nucleation characteristics

3.1.1 Homogeneous nucleation rate

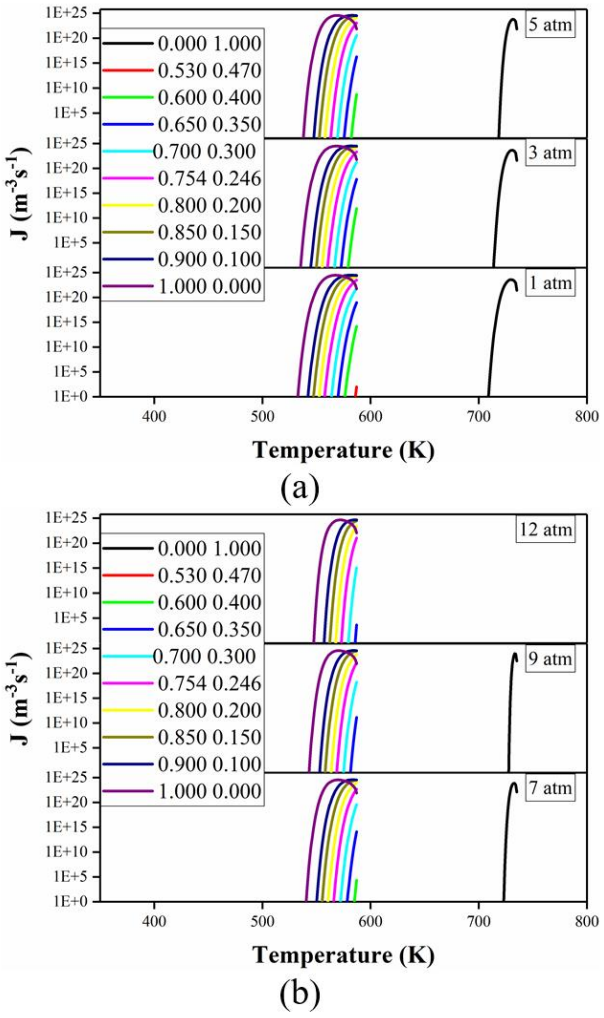

Fig. 7. The influence of environmental pressure on homogeneous nucleation rate.

Fig. 7 shows the change trend of homogeneous nucleation rate J with ambient pressure under different liquid temperatures and compositions. When the n-pentanol fraction pentanol is 0.53, as the ambient pressure increases from 1 atm to 3 atm, the homogeneous nucleation rate J of the blended solution decreases from 101.81 $m^{-3}s^{-1}$ to 0 $m^{-3}s^{-1}$. When the n-pentanol mole fraction is 0.6, as the ambient pressure increases from 1 atm to 7 atm, the homogeneous nucleation rate J of the blended solution decreases monotonically from 1.61×10^{14} $m^{-3}s^{-1}$ to 0 $m^{-3}s^{-1}$. And a minimum n-pentanol mole fraction of 0.65 is required for homogeneous nucleation when the ambient pressure is 12 atm. These findings indicate that for the blends of biodiesel and n-pentanol, the critical n-pentanol mole

fraction for homogeneous nucleation increases with increasing ambient pressure. Compared with atmospheric pressure environment, in real engine operating conditions, more n-pentanol is needed for homogeneous nucleation, which may then make micro-explosions to promote secondary atomization of droplets. As can be seen in this figure, with the increase of ambient pressure, the inhibitory effect of pressure on homogeneous nucleation of blended solutions becomes weaker. When the temperature is 580.15 K, as the pressure increases from 1 atm to 3 atm, J decreases from 8.92×10^{21} $m^{-3}s^{-1}$ to 2.50×10^{21} $m^{-3}s^{-1}$; as the pressure furtherly increases to 5 atm, J decreases to 4.63×10^{20} $m^{-3}s^{-1}$.

3.1.2 Superheating limit temperature

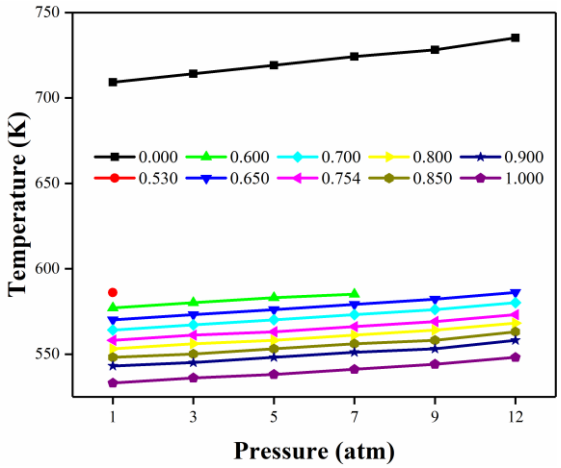

Fig. 8. Change trend of superheating limit temperature.

Fig. 8 shows the change of liquid superheating limit temperature under different ambient pressures and n-pentanol mole fractions. Here, the superheating limit temperature is the liquid temperature corresponding to the homogeneous nucleation rate J of 1 $m^{-3}s^{-1}$. It can be clearly seen from the figure that for the liquid with a certain n-pentanol mole fraction, the superheating limit temperature increases monotonically with the increase of ambient pressure. As mentioned earlier, increasing ambient pressure will lead to an increase in the difficulty of homogeneous nucleation. When the ambient pressure is constant, as the n-pentanol mole fraction increases, the superheating limit temperature of the liquid decreases monotonically. Specifically, it can be observed that when the ambient pressure is 1 atm, as the n-pentanol mole fraction increases from 0 to 0.53, the superheating limit temperature decreases significantly from 709.15 K to 586.15 K. In general, increasing the n-pentanol mole fraction and reducing ambient pressure are beneficial for homogeneous nucleation to generate bubbles, which in turn causes droplet micro-explosions and promotes secondary atomization.

3.2 Homogeneous micro-explosion characteristics

3.2.1 The squared diameter and droplet temperature

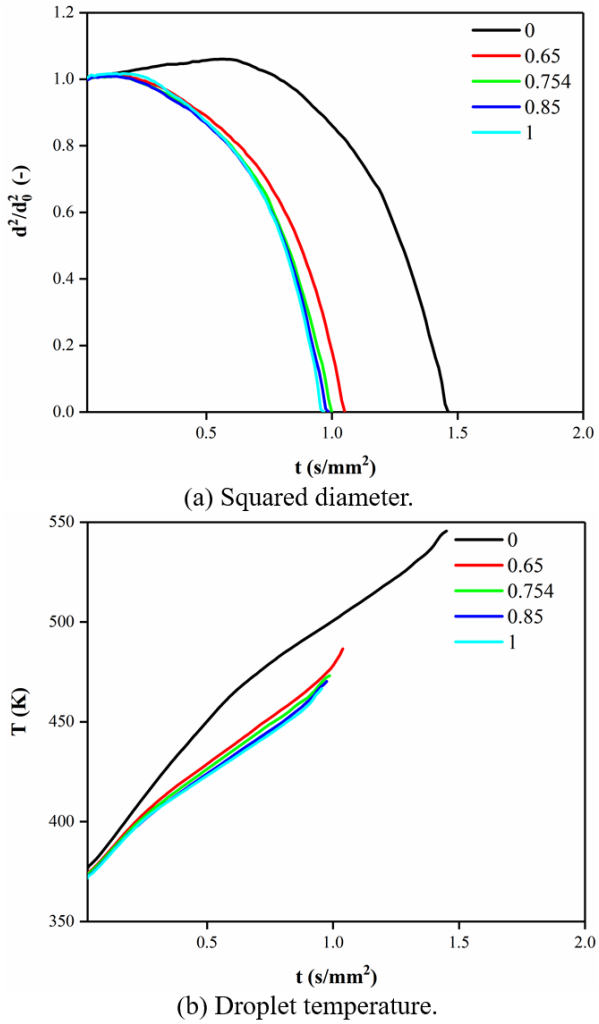

Fig. 9. Changes in the squared diameter and droplet temperature at 1 atm.

Fig. 9 shows the changes of the squared diameter and droplet temperature with liquid composition at 1 atm. From Fig. 9(a), it can be seen that the droplet evaporation curve is similar. As evaporation progresses, the squared diameter increases first and then decreases until the droplet evaporates completely. As the mole fraction of n-pentanol increases, the droplet lifetime monotonically decreases. The change in the squared diameter during evaporation process is mainly influenced by the droplet surface evaporation rate k_v and the droplet thermal expansion rate k_e. For droplets with the 0 n-pentanol mole fraction, the saturated vapor pressure is lower in the early stage of evaporation and then k_v is lower. The density decreases with increasing temperature and k_e is higher, thus the droplet squared diameter increases. As temperature increases, the saturated vapor pressure increases rapidly and k_v is greater than k_e, resulting in a monotonic decrease in the squared diameter. For droplets with a higher n-pentanol

mole fraction, similar to the ones with 0 n-pentanol mole fraction, the initial k_e is larger and dominant, resulting in an increase in the squared diameter. However, at the same temperature, the saturated vapor pressure of n-pentanol is higher than that of biodiesel, and the increase rate of saturated vapor pressure with temperature of n-pentanol is also higher than that of biodiesel, then the surface evaporation rate k_v increases rapidly. Therefore, the duration of the increase in the droplet squared diameter is relatively short, and the droplet lifetime decreases with the increase of n-pentanol content.

As shown in Fig. 9(b), the droplet temperature increases monotonically and shows a three-stage characteristic. In the first stage, the surface evaporation of the droplet is weak and the heat consumed by evaporation is small because of the lower saturated vapor pressure, resulting in a higher temperature rise rate of the droplet. In the second stage, surface evaporation is enhanced as the saturated vapor pressure increases, which results a decrease in the temperature rise rate. In the third stage, the droplet enters the final stage of evaporation and is influenced by the suspension medium. The droplet fluctuates on the suspension medium, enhancing the convective heat transfer between the droplet and the ambient gas. Therefore, the temperature rise rate of the droplet increases until the end of evaporation. As the n-pentanol mole fraction in the droplet increases, the first stage of the droplet gradually shortens. This is because the saturated vapor pressure of n-pentanol is higher than that of biodiesel, and the increase in n-pentanol content leads to enhanced surface evaporation. Meanwhile, due to the higher vaporization latent heat of n-pentanol compared to biodiesel at the same temperature, the average temperature of the droplet is also lower at the same time as the n-pentanol mole fraction increases. Importantly, as shown in Fig. 9(b), the droplet temperature has not reached the superheating limit temperature for homogeneous nucleation when the ambient pressure is 1 atm. Therefore, it is impossible for the droplet to form a homogeneous micro-explosion. Before its temperature reaches the corresponding homogeneous superheating limit temperature, the droplet has already evaporated completely.

Fig. 10 shows the change curves of the squared diameter and droplet temperature with liquid composition at 3 atm. Similar to the curve in Fig. 9(a), the droplet squared diameter increases first and then decreases with time; the difference is that after the pressure increases, the duration of the droplet squared diameter increases and the droplet lifetime increases. This is because as the ambient pressure increases, the partial pressure of biodiesel and n-pentanol vapor correspondingly increases, while the saturated vapor pressure remains constant. Then surface evaporation k_v weakens and the thermal expansion rate k_e is greater than k_v. Unlike that at 1 atm, as the mole fraction of n-pentanol increases, it can be seen that the droplet lifetime decreases first and then increases, reaching its minimum value when the mole fraction of n-pentanol is 0.754. This indicates that after the pressure increases, although the increase of n-pentanol can enhance surface evaporation for the higher saturated vapor pressure, when the content increases to a certain value, the surface evaporation rate is weakened due to the greater latent heat of n-pentanol compared to biodiesel.

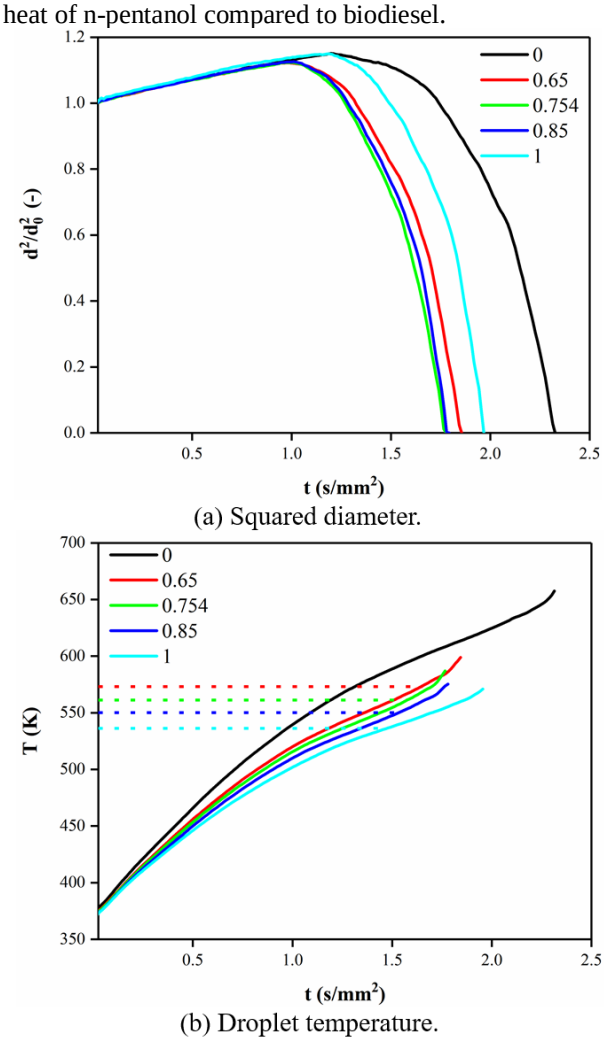

(a) Squared diameter.
(b) Droplet temperature.

Fig. 10. Changes in the squared diameter and droplet temperature at 3 atm.

From Fig. 10(b), the change curve of the droplet average temperature at 3 atm is similar to that at 1 atm. Compared with that at 1 atm, the temperature rise rate is higher when the pressure rises to 3 atm because the weaker evaporation on the droplet surface. The n-pentanol content in the droplet has a more significant effect on its temperature after the pressure increases. More importantly, observing Fig. 10(b), it can be seen that due to the higher vapor partial pressure weakening the evaporation on the droplet surface, the droplet average temperature reaches the superheating limit temperature for homogeneous nucleation. At this point, vapor nuclei can be generated inside the droplet, forming a micro-explosion. Therefore, it can be concluded that increasing ambient pressure is beneficial for homogeneous micro-explosion of droplets.

3.2.2 Vapor

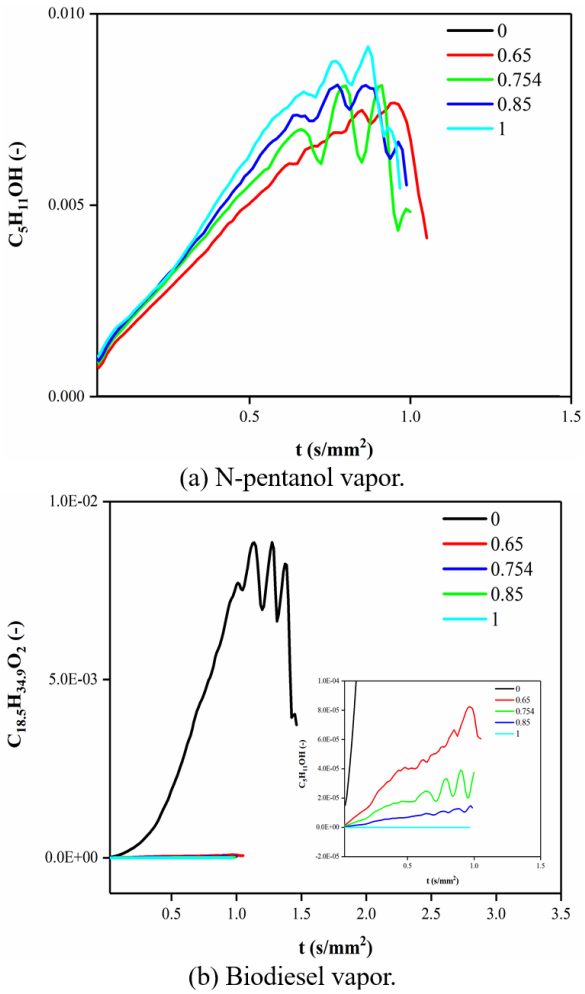

Fig. 11. Changes in vapor mass fraction at 1 atm.

Fig. 11 shows the change of the average mass fraction of n-pentanol and biodiesel vapor in Fluid1 around droplet at 1 atm. As the droplets evaporate, it can be seen from Fig. 11(a) that the average mass fraction of n-pentanol vapor increases smoothly first and then decreases fluctually. According to Fig. 11(b), for droplets with a liquid n-pentanol mole fraction of 0.65 or less, the change of the average biodiesel vapor mass fraction is similar to that of n-pentanol vapor. However, when the mole fraction of n-pentanol is greater than 0.65, there is no fluctuant reduction phenomenon in the later stage of evaporation. This is because as the droplet temperature increases, the saturated vapor pressure of n-pentanol increases rapidly, resulting in an increase in its total evaporation and vapor content. As evaporation proceeds, the partial pressure of n-pentanol vapor gradually increases, and the surface area of droplet evaporation gradually decreases, resulting in a decrease in the total evaporation amount. Meanwhile, vapor continuously diffuses out of Fluid1 region around the droplet, leading to a decrease in the vapor content around the droplet. For biodiesel vapor, it decreases in the later stages of evaporation for similar reasons. When the content of liquid n-pentanol is greater than 0.65, its content remains basically unchanged in the later stage. This is because the content of biodiesel itself in the droplet is relatively small, and its diffusion coefficient is smaller than that of n-pentanol vapor. Then diffusion rate out of Fluid1 region is smaller and it does not decrease sharply in the later stage of evaporation. Due to the lower saturated vapor pressure at the same temperature compared to n-pentanol, as well as lower mole fraction of biodiesel, the content of biodiesel vapor around the droplet is lower than that of n-pentanol vapor at the same evaporation time. As the mole fraction of n-pentanol increases, the average mass fraction of biodiesel vapor decreases monotonically.

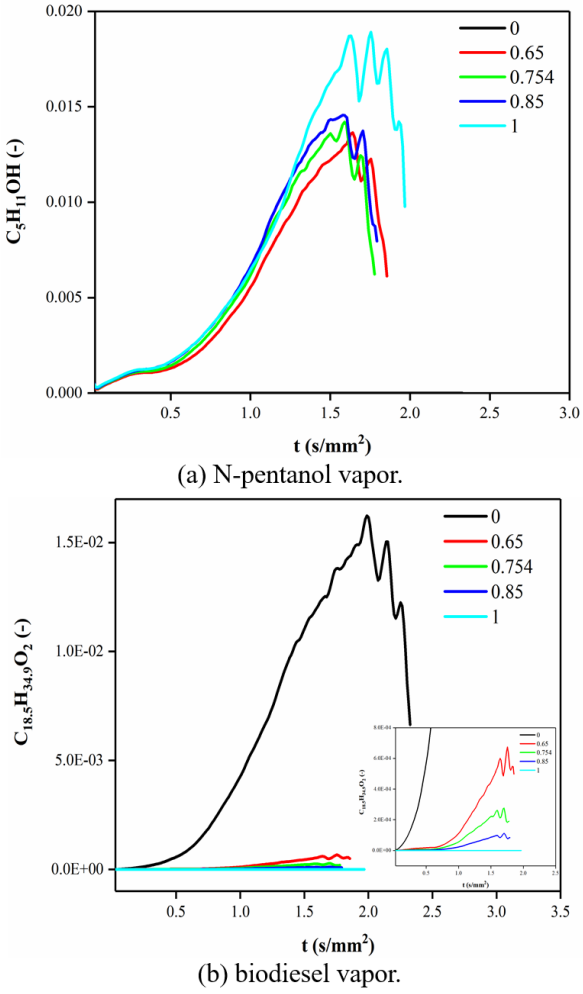

Fig. 12. Changes in vapor mass fraction at 3 atm.

The change of vapor mass fraction at 3 atm is shown in Fig. 12. As shown in Fig. 12(a), the curve is similar that at 1 atm. Compared with that of 1 atm, the increase rate in the mass fraction of n-pentanol vapor is smaller. As mentioned earlier, this is mainly because the partial pressure of vapor is higher under high ambient pressure. Besides, the maximum mass fraction of n-pentanol vapor is higher at 3 atm. Similar to that of 1 atm, the content of n-pentanol vapor increases with the increase of its liquid component mole fraction in the droplet. Observing Fig. 12 (b), the change pattern of biodiesel vapor is similar that of n-pentanol vapor. For biodiesel vapor, the increase rate is smaller and the maximum value is larger

than that at 1 atm. As that at 1 atm, the content of biodiesel vapor decreases with the increase of n-pentanol mole fraction. However, the decrease when n-pentanol mole fraction changes from 0.754 to 0.85 is smaller than that when n-pentanol mole fraction changes from 0.65 to 0.754.

3.2.3 Micro-explosion delay

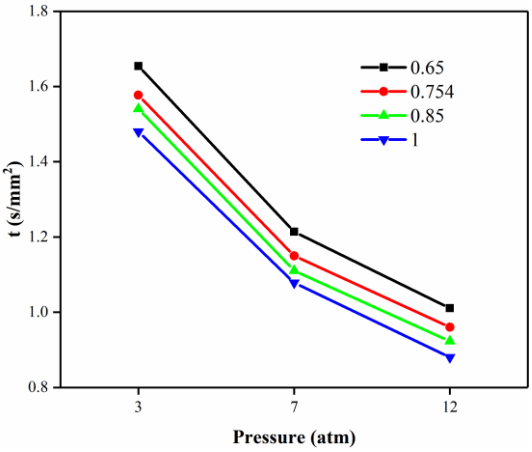

Fig. 13. Effect of pressure on micro-explosion delay.

Fig. 13 shows the change trend of homogeneous micro-explosion delay of droplets under different ambient pressures and n-pentanol mole fractions. In this study, the homogeneous micro-explosion delay is defined as the time interval between the time when the droplet reaches the heating position and the time when its average temperature rises to the homogeneous superheating limit temperature. As shown in the figure, the homogeneous micro-explosion delay decreases with the increase of n-pentanol mole fraction in the droplet. The increase in n-pentanol mole fraction leads to enhanced surface evaporation of the droplet, resulting in lower droplet temperatures and slower temperature rise rates. However, as the n-pentanol mole fraction increases, the homogeneous superheating limit temperature decreases. Then the homogeneous micro-explosion delay decreases. Observing Fig. 13, it can also be seen that with the increase of pressure, the homogeneous micro-explosion delay decreases significantly. As mentioned earlier, the homogeneous superheating limit temperature increases with an increase in pressure. At the same time, the increase in pressure also suppresses the surface evaporation of droplets, which increases the average temperature and temperature rise rate of droplets, thereby reducing the homogeneous micro-explosion delay. Therefore, within the critical temperature and pressure range of n-pentanol, increasing its mole fraction in the blended droplets and ambient pressure is beneficial for the formation of homogeneous micro-explosions for droplets.

4 Conclusions

The effect of pressure on the homogeneous nucleation and evaporation of biodiesel/n-pentanol blended droplets is conduced using the three-dimensional VOF method. The conditions for droplet homogeneous micro-explosion are explored. The main conclusions drawn are as follows:

1. The increase in pressure inhibits the homogeneous nucleation of droplets. That reduces the homogeneous nucleation rate, increases the homogeneous superheating limit temperature, and increases the critical n-pentanol mole fraction for homogeneous nucleation. In this study, a minimum n-pentanol mole fraction of 0.65 is required at 12 atm to form homogeneous nucleation.

2. The increase in pressure weakens the surface evaporation of droplets. That reduces the mass fraction increase rate of biodiesel vapor and n-pentanol vapor, and increases the peak vapor value.

3. Increasing pressure helps to improve droplet temperature and temperature rise rate, resulting in a reduce in the homogeneous micro-explosion delay. It is found that a pressure greater than 3 atm is required for homogeneous micro-explosion.

References

1. LAW C K. Unsteady droplet combustion with droplet heating [J]. Combustion and Flame, 1976.26: 17-22.
2. LAW C K, SIRIGNANO W A. Unsteady droplet combustion with droplet heating—II: Conduction limit [J]. Combustion and Flame, 1977.28: 175-186.
3. ABRAMZON B, SIRIGNANO W A. Droplet vaporization model for spray combustion calculations [J]. International Journal of Heat and Mass Transfer, 1989.32: 1605-1618.
4. BHATTACHARYA P, GHOSAL S, SOM S K. Evaporation of multicomponent liquid fuel droplets [J]. International Journal of Energy Research, 1996.20: 385-398.
5. SEZEN Y. Unsteady mass transfer analysis of evaporation of a single multicomponent droplet with diffusion and constant rate processes [J]. International Communications in Heat and Mass Transfer, 2000.27: 559-568.
6. ZENG Y B, LEE C F. Multicomponent-fuel film-vaporization model for multidimensional computations [J]. JOURNAL OF PROPULSION AND POWER, 2000.16: 964-973.
7. NADYKTO A B, SCHUKIN E R, KULMALA M, et al. Evaporation and condensation rates of a multicomponent droplet in a non-isothermal gas mixture [J]. Journal of Aerosol Science, 2000.31: 801-802.
8. SAZHIN S S, ELWARDANY A, KRUTITSKII P A, et al. A simplified model for bi-component droplet heating and evaporation [J]. International Journal of Heat and Mass Transfer, 2010.53: 4495-4505.
9. SAZHIN S S, ELWARDANY A E, KRUTITSKII P A, et al. Multi-component droplet heating and evaporation: Numerical simulation versus

experimental data [J]. International Journal of Thermal Sciences, 2011.50: 1164-1180.

10. BANERJEE R. Numerical investigation of evaporation of a single ethanol/iso-octane droplet [J]. Fuel, 2013.107: 724-739.
11. STROTOS G, GAVAISES M, THEODORAKAKOS A, et al. Numerical investigation of the evaporation of two-component droplets [J]. Fuel, 2011.90: 1492-1507.
12. KAIHAN, QIZHAOLIN, MINGHOULIU, et al. Experimental study on the micro-explosion characteristics of two blended types of droplets under different nitrogen flow rates [J]. Physics of Fluids, 2022.34: 033609.
13. HUANG X, WANG J, WANG Y, et al. Experimental study on evaporation and micro-explosion characteristics of biodiesel/n-propanol blended droplet [J]. Energy, 2020.205: 118031.
14. LI F Y, TIAN J J, HAN K, et al. Expansion and combustion of droplets that contain long-chain alcohol alternative fuels [J]. Physics of Fluids, 2021.33.
15. QIU Z, TIAN J, LIU Y, et al. Influence of micron-sized aluminum particles on micro-explosion and combustion characteristics of ethanol-biodiesel droplets under co-heat flow [J]. Fuel, 2022.326: 124877.
16. QIU Z, TIAN J, LIU Y, et al. Expansion/micro-explosion of ethanol-biodiesel droplet doped with microparticles in oxygenated hot co-flow [J]. Applied Thermal Engineering, 2023.221: 119345.
17. LIANG J C, ZHANG Q C, CHEN Z, et al. The effects of EGR rates and ternary blends of biodiesel/n-pentanol/diesel on the combustion and emission characteristics of a CRDI diesel engine [J]. Fuel, 2021.286.
18. MENG K, FU W, LEI Y, et al. Study on micro-explosion intensity characteristics of biodiesel, RP-3 and ethanol mixed droplets [J]. Fuel, 2019.256: 115942.
19. MENG K, FU W, LI F, et al. Comparison of ignition, injection and micro - Explosion characteristics of RP-3/ ethanol and biodiesel / ethanol mixed drops [J]. Journal of the Energy Institute, 2020.93: 152-164.
20. MENG K, HAN K, LI F, et al. Study on combustion and micro-explosion characteristics of biodiesel and ethanol mixture droplets under different oxygen concentrations and temperatures [J]. Physics of Fluids, 2021.33: 052003.
21. MENG K S, BAO L, SHI Y B, et al. Experimental investigation on ignition, combustion and micro-explosion of RP-3, biodiesel and ethanol blended droplets [J]. Applied Thermal Engineering, 2020.178.
22. MENG K S, FU W, LI F Y, et al. Expansion, injection and micro-explosion phenomena during the full combustion cycle of mixed fuel droplets of ethyl alcohol and biodiesel [J]. Combustion Theory and Modelling, 2020.24: 810-828.
23. MENG K S, WU Y K, LIN Q Z, et al. Microexplosion and ignition of biodiesel/ethanol blends droplets in oxygenated hot co-flow [J]. Journal of the Energy Institute, 2019.92: 1527-1536.
24. GANESAN N, LE T H, EKAMBARAM P, et al. Experimental assessment on performance and combustion behaviors of reactivity-controlled compression ignition engine operated by n-pentanol and cottonseed biodiesel [J]. Journal of Cleaner Production, 2022.330.
25. PAN M Z, HUANG R, LIAO J Y, et al. Experimental study of the spray, combustion, and emission performance of a diesel engine with high n-pentanol blending ratios [J]. Energy Conversion and Management, 2019.194: 1-10.
26. ZHANG Y, HUANG R, ZHOU Y, et al. Effects of turbulence intensity and n-pentanol concentration on droplet evaporation and auto-ignition [J]. Fuel, 2022.322: 124177.
27. LI F Y, SHI W D, HU C, et al. Global characteristics of transverse jets of aviation kerosene-long-chain alcohol blends [J]. Physics of Fluids, 2020.32.
28. HAN K, LIN Q Z, LIU M H, et al. Experimental study on the micro-explosion characteristics of biodiesel/1-pentanol and biodiesel/ methanol blended droplets [J]. Renewable Energy, 2022.196: 261-277.
29. LEE C F F, WANG K T, CHENG W L. Atomization Characteristics of Multi-component Bio-fuel Systems under Micro-explosion Conditions; proceedings of the Sae World Congress & Exhibition, F, 2008 [C].
30. ZENG Y, LEE C-F F. Modeling droplet breakup processes under micro-explosion conditions [J]. Proceedings of the Combustion Institute, 2007.31: 2185-2193.
31. AVEDISIAN C T. The Homogeneous Nucleation Limits of Liquids [J]. Journal of Physical and Chemical Reference Data, 1985.14: 695-729.